nature chemistry

Article

https://doi.org/10.1038/s41557-026-02070-4

Homochiral toroidal spin state in Dy(III)-based single-molecule toroics

Received: 6 February 2024

Accepted: 13 January 2026

Published online: 23 February 2026

Check for updates

Zhenhua Zhu[1,8], Xu Ying[1,2,8], Langit Cahya Adi[3], Chen Zhao[1], Elizabeth Jia Mei Chew[4], Liviu Ungur[4], Sagar Paul[5], Wolfgang Wernsdorfer[5,6], Cyrille Train[3], Geert L. J. A. Rikken[3], Matteo Atzori[3] ✉ & Jinkui Tang[1,2,7] ✉

Single-molecule toroics, materials that combine spin and chirality at the molecular level, are promising candidates for applications in data storage, chiral spintronics and magnetoelectric devices. Over the past two decades, substantial progress has been made in the design of toroidal spin states via ligand design and coordination chemistry strategies. However, achieving homochiral magnetic vortex configurations across both molecular and unit-cell scales—a key prerequisite to induce the toroidal polarization using a homogeneous magnetic field—remains challenging. Here we report enantiopure chiral dysprosium triangles in which introduction of structural chirality induces spin homochirality. μ-SQUID magnetometry and ab initio calculations evidence a non-coplanar spin texture that exhibits a toroidal ground state at low temperature. Furthermore, magneto-chiral dichroism spectroscopy, a technique sensitive to both chirality and magnetization, reveals unusual behaviours below 4.5 K, the temperature at which the coupling between Dy(III) ions favours the generation of a toroidal spin state.

Chirality, by breaking mirror symmetry, plays a fundamental role across physics, chemistry and biology, manifesting at all scales, from biologically important molecules (for example, chiral amino acids) to galactic structures (for example, spiral galaxies). In the field of condensed matter physics, various types of topological spin texture, like skyrmions[1,2], merons or antimerons[3] and recently discovered hopfion rings[4], have been observed in bulk chiral crystals or chiral hybrid materials. Spin, an intrinsic quantum property of the electron, is equally central to the stability and fundamental properties of matter[5]. Control over electronic spin states via microwave pulses, electric and/or magnetic fields and ligand engineering makes spin a highly versatile platform for quantum technologies, advanced solid-state systems and tailored molecular materials[6,7]. The interplay between chirality and electronic spin underpins abundant physical and optical phenomena with appealing potential in chiral spintronics. Prominent examples include chiral superconductor[8] and spin light-emitting diode[9], both of which take advantage of chirality-induced spin selectivity effect[10], which refers to enantiopure non-magnetic chiral organic molecules that act as spin filters to induce electron spin polarization.

Spin chirality—arising from non-collinear (vector spin chirality) and non-coplanar (scalar spin chirality) arrangements of spins—has attracted much attention recently for its crucial roles in topological physics, quantum engineering and spintronics[11,12]. Toroidal moments (Fig. 1a,b)[13], generated by the non-collinear head-to-tail arrangement of magnetic moments, offer a robust pathway to attain spin chirality as they have a profound correspondence (Fig. 1c); for example, they are

[1]State Key Laboratory of Rare Earth Resource Utilization, Changchun Institute of Applied Chemistry, Chinese Academy of Sciences, Changchun, P. R. China. [2]School of Chemistry and Chemical Engineering, Beijing Institute of Technology, Beijing, P. R. China. [3]Laboratoire National des Champs Magnétiques Intenses (LNCMI), CNRS, Univ. Grenoble Alpes, INSA Toulouse, Univ. Toulouse Paul Sabatier, EMFL, Grenoble, France. [4]Department of Chemistry, National University of Singapore, Singapore, Singapore. [5]Physikalisches Institut, Karlsruhe Institute of Technology (KIT), Karlsruhe, Germany. [6]Institute for Quantum Materials and Technology (IQMT), Karlsruhe Institute of Technology (KIT), Eggenstein-Leopoldshafen, Germany. [7]University of Science and Technology of China, Hefei, P. R. China. [8]These authors contributed equally: Zhenhua Zhu, Xu Ying. ✉e-mail: matteo.atzori@lncmi.cnrs.fr; jtang@bit.edu.cn

https://doi.org/10.1038/s41557-026-02070-4

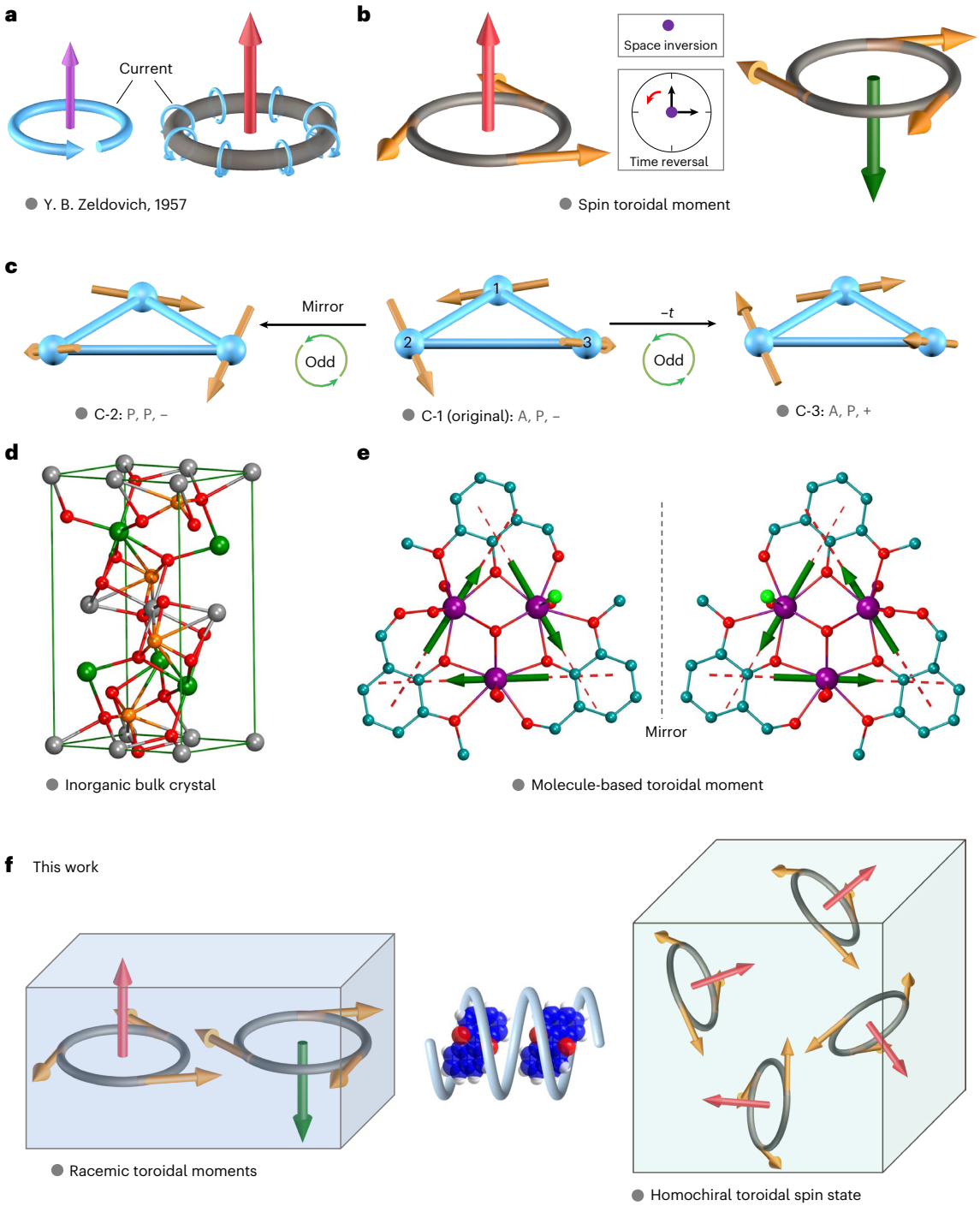

Fig. 1 | Toroidal moment and spin chirality. a, Current windings on the surface of toroid along its meridians producing polar (magnetic) toroidal moment[13]. **b**, Toroidal magnetic dipole moment arising from vortex-like configurations of spin and its transformation properties under space–time parity operations. **c**, Toroidal moment, vector spin chirality and scalar spin chirality made by three non-coplanar spins on an equilateral triangle. C-2 and C-3 are obtained by the mirror operation and time reversal of C-1, respectively. The symbols, 'P and A', represent the directions of toroidal moment ($\mathbf{T} = \sum_{i=1,2,3} \mathbf{r}_i \times \mathbf{S}_i$, where $\mathbf{S}_i$ and $\mathbf{r}_i$ are the spin and position of the ith Dy ion in the triangle) and vector spin chirality ($\boldsymbol{\kappa} = \mathbf{S}_1 \times \mathbf{S}_2 + \mathbf{S}_2 \times \mathbf{S}_3 + \mathbf{S}_3 \times \mathbf{S}_1$) with respect to the net spin magnetic moment ($\mathbf{S} = \sum_{i=1,2,3} \mathbf{S}_i$), respectively, 'P' for parallel and 'A' for antiparallel, while '+' and '−' indicate the sign of the scalar spin chirality ($\chi = \mathbf{S}_3 \cdot \mathbf{S}_1 \times \mathbf{S}_2$). **d**,**e**, Solid structures of $LiCoPO_4$ (ref. 19) (**d**) and **Dy_3-1** (ref. 22) (**e**) as well as the racemic spin chirality in the unit cell of **Dy_3-1**. Green arrows represent the direction of ground-state magnetic anisotropy axis of local Dy(III) sites. **f**, Schematic representation of the chirality-induced purification of toroidal moments. Yellow arrows represent spin magnetic moments, while red and green arrows represent the toroidal moments. Panels adapted with permission from: **d**, ref. 19 under a Creative Commons licence CC0 1.0; **e**, ref. 22, Wiley.

odd under time reversal symmetry[14–16]. When toroidal moments are all aligned along the same direction, the system exhibits ferrotoroidicity—the fourth form of ferroic order, along with ferromagnetism, ferroelectricity and ferroelasticity[17]. This ferro-magnetic-toroidal order can change sign under both time reversal and spatial inversion, showing exceptional promise for magnetoelectric coupling[18]. Compared with inorganic toroidal materials, for example $LiCoPO_4$ (refs. 17,19) (Fig. 1d), $LiFeSi_2O_6$ (ref. 20) and $BaCoSiO_4$ (ref. 21), molecule-based toroidal

https://doi.org/10.1038/s41557-026-02070-4

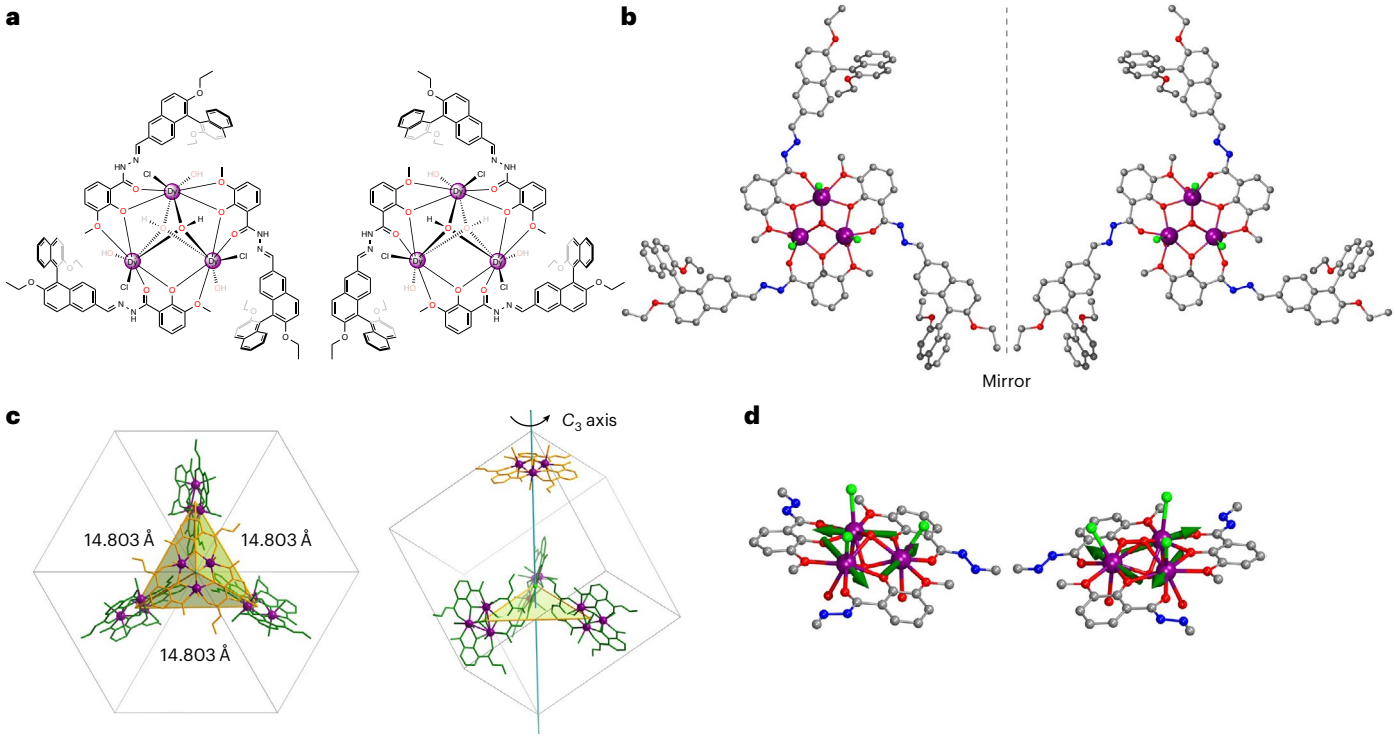

Fig. 2 | Structures and toroidal arrangement of magnetization. a,**b**, Chemical and crystal structures of **R-Dy$_3$** (**a**) and **S-Dy$_3$** (**b**). Dy, purple; N, blue; O, red; C, dark grey; Cl, bright green. Non-coordinating anions and solvent molecules as well as hydrogen atoms are omitted for clarity. **c**, Molecular packing in the cubic unit cell featuring a C_3 rotation axis along the body diagonal. The yellow molecule is parallel to (111) plane while the other three green molecules are approximatively perpendicular to it. **d**, Toroidal spin ground state in **R-Dy$_3$** (left) and **S-Dy$_3$** (right). Green arrows represent the directions of ground-state main magnetic axes for local Dy(III) ions determined by ab initio calculations. The BINOL derivates are omitted for clarity.

moments, called single-molecule toroics (SMTs), have distinct advantages in tuning topological and electronic structures by virtue of the versatility of coordination chemistry. In 2006, one study reported a triangular Dy(III)-based SMT, $(Dy_3L^1{}_3(\mu_3\text{-}OH)_2Cl(H_2O)_5)\cdot 3Cl$ (HL^1, *o*-vanillin, **Dy$_3$-1**) (Fig. 1e), which was prepared in mild synthetic conditions: that is, room-temperature solution synthesis[22]. Theoretical investigations revealed that the principal axes of the ground Kramer doublet of three Dy(III) ions are all oriented along the $O_{phenolate}$–Dy-$O_{phenolate}$ direction, out of the Dy_3 plane, forming a non-coplanar toroidal arrangement via Dzyaloshinskii–Moriya interactions[23]. Since then, various types of SMTs with the Dy_3 motif have been prepared to get insight into the toroidal spin state nature[24]. In 2012, another research group reported on the compound $(Dy_3(H_2L^2)(HL^2)(NO_3)_4)$ (H_4L^2, *N*,*N*,*N*,*N*-tetrakis (2-hydroxyethyl)-ethylenediamine, **Dy$_3$-2**) that crystallizes in a polar space group, $Pna2_1$, and exhibits SMT and single-molecule magnet behaviours as well as ferroelectricity[25]. In 2017, one study revealed that heterometallic complex, $(Cr^{III}Dy^{III}{}_6(OH)_8(L^3)_{12}(NO_3)(MeOH)_5)\cdot 3MeOH$ (HL^3, 2-methylbenzoic acid, **Dy$_6$Cr**), possesses an enhanced toroidal moment due to the presence of ferrotoroidic ground state[26]. Recently, one research group disclosed that SMT behaviour can also be observed in a tridimensional Dy_4 cubane[27]. In addition, the scope was also broadened to Tb(III)-based SMTs, for example Tb_6Cu_6 metallacycle and covalently bonded Tb-TC4A (H_4TC4A, *p*-tert-butylthiacalix(4)arene) polymers[28,29].

Although substantial progress in the synthesis of SMTs with diverse shapes and tunable magnetic properties were made, all reported SMTs except for one-dimensional $(Cu(L^4)_2CH_3OH)(L^1{}_3Dy_3(\mu_3\text{-}OH)_2(NO_3)_4)_n$ (HL^4, enantiopure valine, **Dy$_3$Cu**) compound crystallized in achiral space groups; that is, the toroidal ground spin states in the unit cell adopts 50% clockwise orientations and 50% anticlockwise orientations (Fig. 1e and Supplementary Table 1). Although **Dy$_3$Cu** crystallized in a chiral space group, $P2_1$, the presence of paramagnetic Cu(II) ion and an additional racemization deriving from the Δ and Λ arrangements of the main part of the chains in a given enantiomer leads to the absence of pure toroidal spin states and reduced chiral effects, respectively[30]. In addition, some highly symmetrical metallacycles are *meso* species due to the presence of rotation–reflection axis, S_n, for example S_6 in $(Dy(HL^5)(NO_3))_6\cdot 8MeOH$ (H_3L^5, triethanolamine, **Dy$_6$-1**)[31] and Tb_6Cu_6 (ref. 28), giving a net zero toroidal moment. Therefore, in such systems, the application of a magnetic field gradient to engineer a homochiral toroidal configuration is necessary for inducing toroidal polarization: a prerequisite for magnetoelectric coupling and electric manipulation[32]. However, it is a formidable challenge to implement such inhomogeneous magnetic fields at the molecular level. Recently, Hymas and Soncini proposed an alternative protocol, that is using pulsed microwaves to selectively and coherently prepare and manipulate molecular toroidal moments without requiring static magnetic field gradients[33]. A key requirement for this protocol is the presence of weak inversion symmetry breaking in the molecule. Thus, constructing homochiral SMTs is crucial to maximize toroidal polarization. Furthermore, the vanishingly small total magnetization in the ground state of SMTs renders the experimental detection of the toroidal spin states another considerable challenge via classical magnetometry and related thermodynamic techniques. Considering the coexistence of structural chirality and spin chirality in enantiopure SMTs, magneto-chiral dichroism (MChD) spectroscopy, simultaneously sensitive to chiral features and the magnetization of matter, could be a powerful probe to detect non-coplanar spin textures[34,35].

Herein, we synthesized an enantiomeric pair of 0D SMTs, **R/S-Dy$_3$**, by the coordination-driven self-assembly between Dy(III) ion and enantiopure 1,1′-Bi-2-naphthol (BINOL)-modified hydrazone ligands. The compounds possess a triangular Dy_3 core as the sole magnetic source, showing spin homochirality imposed by the introduction of structural chirality (Fig. 1f). At low temperature, a toroidal ground

https://doi.org/10.1038/s41557-026-02070-4

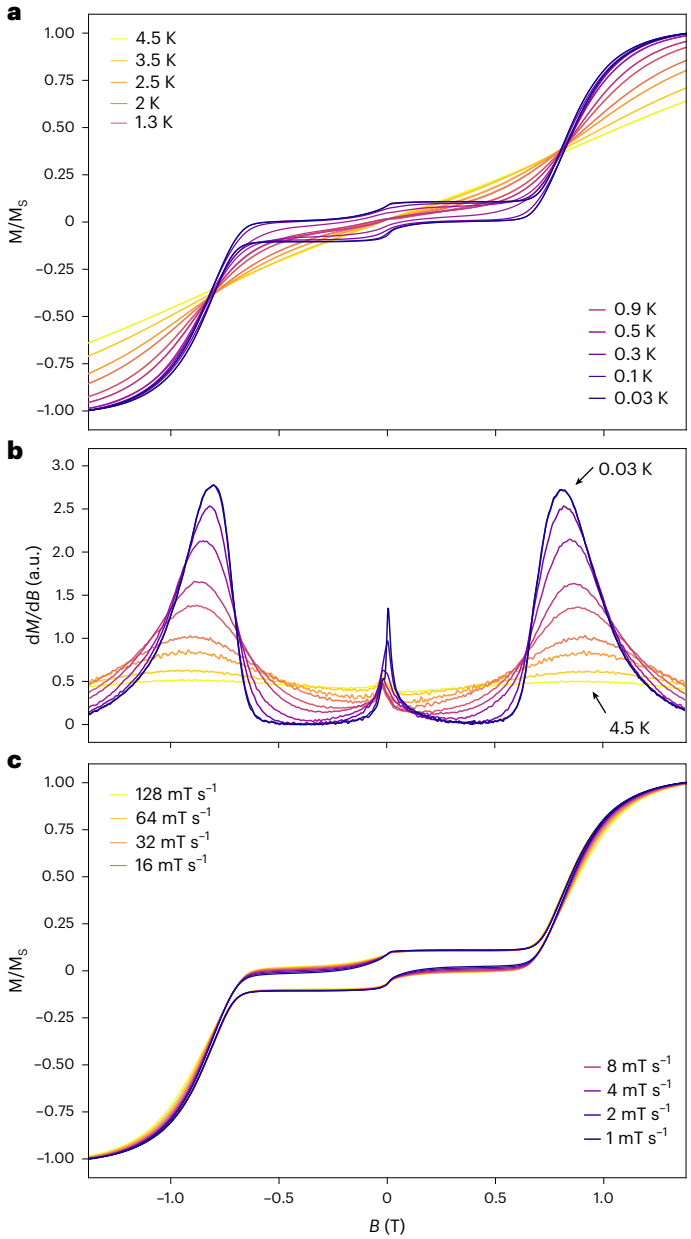

Fig. 3 | Magnetic hysteresis in a single crystal of R-Dy$_3$ measured by μ-SQUIDs. **a**, $M(B)$ loops in the temperature range of 30 mK to 4.5 K at 8 mT s^{-1}. **b**,**c**, The corresponding derivatives dM/dB(B) (**b**) and $M(B)$ loops at 30 mK (**c**) with different field sweep rates.

spin state is unambiguously observed by μ-SQUID measurements and supported by ab initio calculations. Moreover, variable-temperature and variable-magnetic-field MChD spectroscopy investigations were conducted to get insight into the orientation and the properties of the toroidal spin state in these compounds: information that cannot be provided by μ-SQUID measurements.

Results and discussions

Synthetic strategy

We selected ethyl-protected chiral BINOL derivatives, (*R*)/(*S*)-2,2′-diethoxy-(1,1′-binaphthalene)-6-carbaldehyde, as the chiral source. Ethylation prevents coordination of two hydroxyl groups to Dy(III) ions (avoiding forming analogues of Shibasaki's heterobimetallic complexes[36]) and enhances acid tolerance compared with methoxymethyl protection. The aldehyde group at the 6-carbon position enables a facile imine condensation with hydrazide-modified *o*-vanillin, affording a pair of hydrazide enantiomers, (*R*)/(*S*)-*N*′-((2,2′-diethoxy-(1,1′-binaphthalen)-6-yl)methylene)-2-hydroxy-3-methoxybenzohydrazide, **R/S-HL** (Supplementary Figs. 1–4). Treatment of **R/S-HL** with $DyCl_3{\cdot}6H_2O$ in the presence of Et_3N in CH_3OH/CH_3CN mixed solvent at room temperature gives the triangular Dy(III)-based trimers, $(Dy_3(R/S\text{-}L)_3(\mu_3\text{-}OH)_2Cl_3(H_2O)_3)Cl{\cdot}9DMF{\cdot}6H_2O$, **R/S-Dy$_3$** (Fig. 2a and Supplementary Scheme 1).

Structural and spectroscopic characterizations

Light-yellow block single crystals of **R/S-Dy$_3$** suitable for single-crystal X-ray diffraction (SCXRD) were obtained by the slow diffusion of diethyl ether into dimethylformamide solution. The SCXRD analysis revealed that they crystallized in a chiral space group, $P2_13$ (Supplementary Table 2). Given that the first coordination environments of Dy(III) ions in enantiomers are almost identical within experimental uncertainties (Supplementary Tables 3 and 4), here we only described the structural details of **R-Dy$_3$**. The complex has a C_3 rotation axis passing through two μ_3-OH that locates above and below the Dy_3 plane with distances of 1.101 Å and 1.155 Å from the plane, respectively (Fig. 2b and Supplementary Figs. 12 and 13). Therefore, the three Dy(III) ions form a strictly equilateral triangle with an edge length of 3.511 Å, corresponding to the intramolecular Dy···Dy distances. Due to the presence of only one free chloride ion as counterion, the trimer is a cationic species with +1 charge, which means that the hydrazide ligand is singly protonated with non-deprotonated NH sites. Every Dy(III) is eight-coordinated with triangular dodecahedron coordination geometry (D_{2d}) surrounded by four oxygen atoms from two L ligands, two μ_3-OH, one chloride ion and one water molecule (Supplementary Fig. 14 and Supplementary Table 5). The 7 Dy–O distances average to 2.352 Å with two Dy–$O_{phenolate}$ distances amounting to 2.366(10) Å and 2.348(9) Å. The bond length of Dy–Cl is obviously longer than that of Dy–O, approaching 2.60 Å. The O–Dy–O bond angles are in the range of 58.2(5)°–153.0(4)°, where the $O_{phenolate}$–Dy–$O_{phenolate}$ angle is 143.7(3)°. The SCXRD analysis evidences the presence of disordered solvent molecules in the unit cell that cannot be easily modelled. Therefore the SQUEEZE subroutine in PLATON was used to mask the corresponding electron density[37]. The number of the electrons in one void per unit cell is consistent with nine dimethylformamide (DMF) and six H_2O molecules, which is in agreement with elemental analyses.

The crystal packing of **R/S-Dy$_3$** shows that the shortest intermolecular Dy···Dy distances are 12.896 Å and 12.929 Å, respectively, indicating relatively weak intermolecular magnetic interactions (Supplementary Figs. 15 and 16). Notably, the symmetry elements of the cubic space group impose that four crystallographically equivalent molecules ($Z = 4$) occupy different positions of the unit cell (Fig. 2c). One molecule has the Dy_3 triangular plane parallel to the (111) crystallographic plane, while the remaining three molecules, which are symmetry-related by a threefold axis perpendicular to (111), display their Dy_3 triangular planes predominantly perpendicular to it (roughly 70°) (Supplementary Fig. 17). The phase purities of **R/S-Dy$_3$** were carefully checked by performing powder X-ray diffraction experiments to ensure the validity of the following spectroscopic studies and magnetic measurements. The obtained patterns, as shown in Supplementary Fig. 5, revealed excellent matches to the simulated ones. The electrospray ionization mass spectra (ESI-MS) in CH_3OH solution (Supplementary Fig. 6), shows a series of sharp +3 charged isotopic peaks corresponding to various Dy_3 motifs, where the strongest signal arises from $(Dy_3(R\text{-}L)_3(\mu_3\text{-}OH)_2(OH)(CH_3OH)_2)^{3+}$ species. This indicates a remarkable robustness of the Dy_3 core even in solution. The UV-vis absorption spectra of **R/S-Dy$_3$** exhibit a distinct red shift with the absorption edge at roughly 420 nm ascribed to the deprotonation and the coordination to Dy(III) ion of the phenolic hydroxyl group (Supplementary Figs. 7–9)[38] with respect to the free **R/S-HL** ligands. The natural circular dichroism spectra of **R/S-Dy$_3$** are mirror images of each other and show similar features with respect to those of **R/S-HL**

https://doi.org/10.1038/s41557-026-02070-4

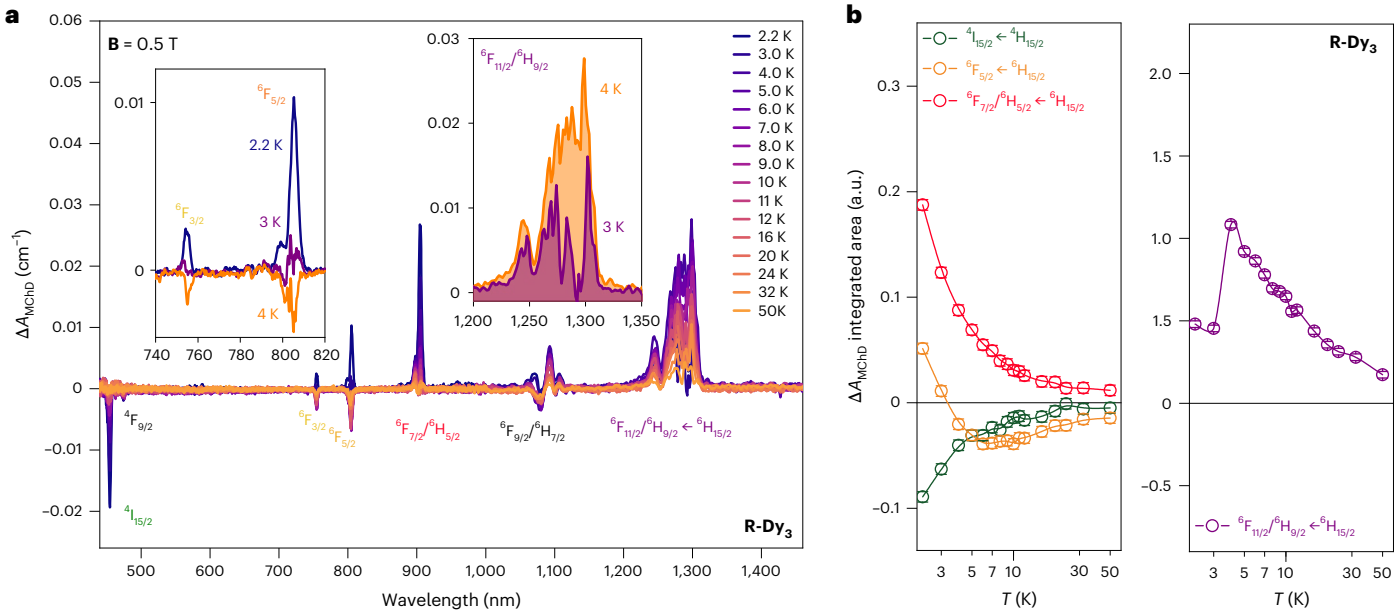

Fig. 4 | Temperature-dependent MChD spectroscopy. a, Variable-temperature MChD spectra for **R-Dy$_3$** at **B** = 0.5 T (**k**,**B** ⊥ (111)) where the differences in MChD signals intensity and sign below 5 K are highlighted (insets). **b**, Temperature (*T*) dependence of the *f*–*f* electronic transitions with the highest ΔA_{MChD} values. The solid lines are used solely as visual guides. Error bars represent ±2σ uncertainty in the integrated signal area.

(Supplementary Figs. 10 and 11). In addition, this system exhibits four types of chiral feature (see details in Supplementary Fig. 18).

SMTs behaviour

To verify the toroidal arrangement of the magnetic anisotropy axes in the ground state of **R/S-Dy$_3$**, magnetic measurements in both the solid and in solution were performed. The $\chi_M T$ (where χ_M is molar magnetic susceptibility) products at 300 K of **R/S-Dy$_3$** are 42.03 cm^3 mol^{-1} K and 41.78 cm^3 mol^{-1} K, which are in excellent agreement with the expected value for three isolated Dy(III) ions ($^6H_{15/2}$, $S = 5/2$, $L = 5$, $J = 15/2$ and $g = 4/3$) (Supplementary Figs. 19 and 20). On cooling, the $\chi_M T$ values decreased gradually from 300 K to 24 K and then dropped rapidly to 3.98 cm^3 mol^{-1} K and 3.77 cm^3 mol^{-1} K at 2.0 K, respectively, indicating the thermal depopulation of the excited M_J (the projection of total angular momentum *J* along the z axis) sublevels of Dy(III) ion and antiferromagnetic couplings within the complexes at low temperature. A peak at roughly 5 K in χ_M versus *T* plots and a sigmoidal shape at low magnetic fields in magnetization (*M*) vs magnetic field (*B*) (*M*(*B*)) curves at 1.9 K (Supplementary Figs. 21 and 22) closely resemble those of **Dy$_3$-1** compound[22], confirming the toroidal arrangement of magnetization in the ground state at low temperature. The saturation values of magnetization at 1.9 K and 7 T are 15.66 μ_B and 15.52 μ_B for **R-Dy$_3$** and **S-Dy$_3$**, respectively. These values are expected for the saturated magnetization of a powder sample for a highly anisotropic molecule containing three Dy(III) ions (in this situation, $M_{sat,Dy}$ is 5 μ_B)[27,39–41]. This lack of saturation and the non-superposition of *M* versus *B*/*T* data indicate the strong magnetic anisotropy and/or low-lying excited states in these two complexes (Supplementary Figs. 23 and 24)[42]. These features were also well reproduced in CH_3OH solution ($c = 8.3$ mM), demonstrating the molecular origin of these phenomena (Supplementary Figs. 27–31). For example, the magnetic hysteresis of **R-Dy$_3$** in crystalline phase and amorphous frozen CH_3OH solution at 1.9 K show the same inflection at ±0.9 T (Supplementary Figs. 25–30), which clearly corroborated the dominant contribution of the local crystal field rather than intermolecular magnetic interactions to the ground state.

Alternating current (a.c.) susceptibility measurements of the two enantiomeric complexes were also carried out to evaluate their magnetization dynamics (Supplementary Figs. 31–36). The temperature-dependent out-of-phase susceptibilities $\chi''(T)$ of both compounds showed the same highest peak temperature (1,488 Hz) of roughly 4 K, while the frequency-dependent signals $\chi''(\nu)$ displayed broad shoulders between 1.9 K and 3.0 K, suggesting the presence of multiple relaxation processes. This was verified by fitting $\chi''(\nu)$ data in this range with a two-step relaxation model[43,44]. The relaxation times extracted from the above fitting were not entirely reliable due to the absence of maxima in $\chi''(\nu)$ plots above 3 K. Therefore, the magnetization decay measurements on single crystals of **R/S-Dy$_3$** via μ-SQUID were conducted to obtain more reliable relaxation times. The radii of the semicircles in Cole–Cole diagrams increase with temperature from 1.9 K to 4.5 K (Supplementary Figs. 33 and 36), an anomalous dynamic behaviour also observed in other antiferromagnetically coupled systems[45,46]. This indicates the relaxation of the magnetization below 4.5 K occurs between a toroidal ground state and non-toroidal excited states.

Low temperature μ-SQUID studies on single crystals of **R/S-Dy$_3$** were performed to (1) further prove the presence of the toroidal arrangement; (2) accurately determine the crossing magnetic field between the toroidal moment regime and a spin-flip state and (3) evaluate the energy gap between the ground toroidal state and the non-toroidal excited state (Fig. 3 and Supplementary Fig. 37). The *M*(*B*) hysteresis loops exhibited a wide plateau between ±0.65 T, confirming the toroidal moment features. Furthermore, the loops exhibit temperature-dependent sharp steps at crossing fields, for example ±0.8 T at 0.03 K and ±0.9 T at 2.0 K, which are due to the crossing of the ground toroidal state to the first excited state stabilized by the Zeeman effect. At 0.03 K, 10% remanent magnetization persists near zero field due to the non-zero total magnetic moment caused by the non-planar spin texture in the ground state (Fig. 3a). Magnetization decay experiments were performed from 0.03 K to 0.5 K (Supplementary Fig. 38). The mean relaxation times were determined by rescaling the time axis to obtain a master curve[47,48] and plotted as $\ln(\tau)$ versus $1/T$ (Supplementary Fig. 39). Fitting the whole temperature range to the equation $\ln(\tau) = -\ln(\tau_0^{-1}\exp(-U_{eff}/k_BT) + CT^n + 1/\tau_{QTM})$ (where U_{eff} is the effective energy barrier, τ_0 is the attempt time, k_B is the Boltzmann constant, *C* and *n* are the Raman prefactor and exponent, respectively, and τ_{QTM} is the quantum tunnelling time) gives $U_{eff} \approx 5.43$ K for both compounds (see Supplementary Fig. 39 for full fitting results).

https://doi.org/10.1038/s41557-026-02070-4

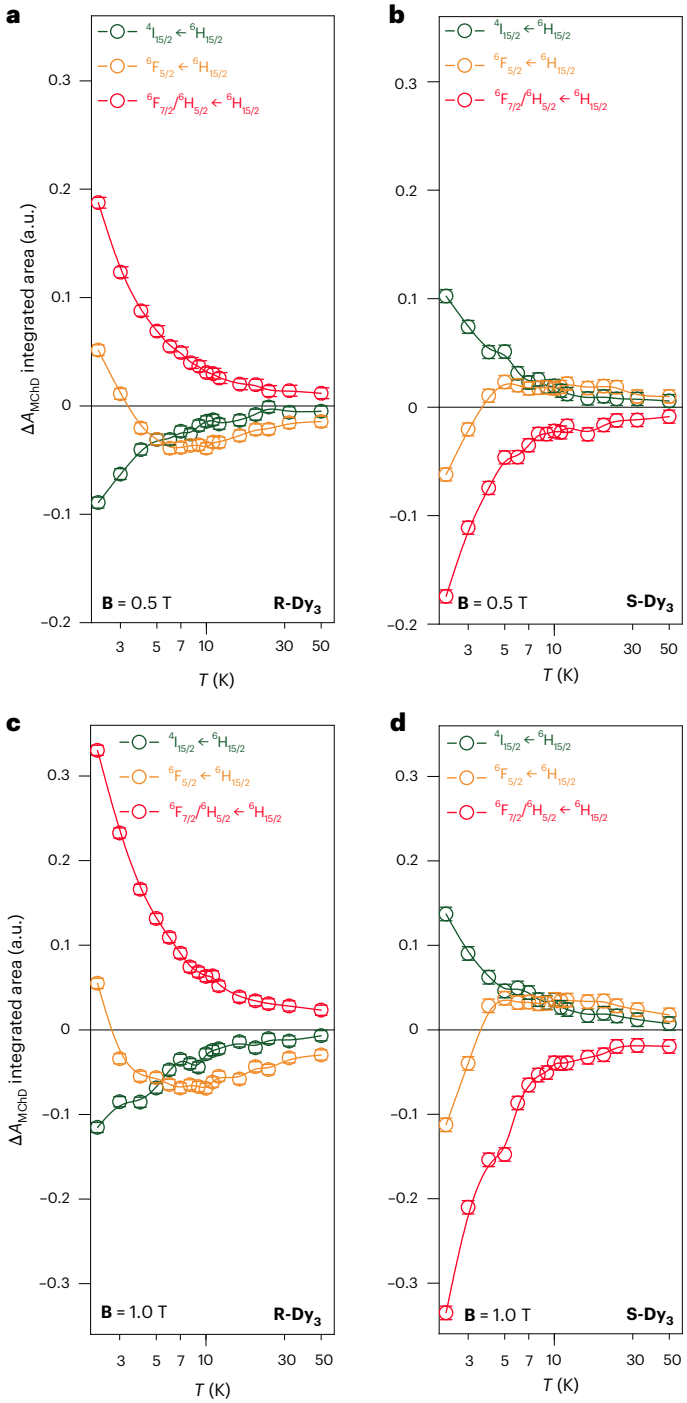

Fig. 5 | MChD response of the two enantiomers as a function of the temperature. **a**–**d**, Temperature dependence of MChD intensity (integrated absolute area of the MChD signals) for the two enantiomers **R-Dy$_3$** (**a**,**c**) and **S-Dy$_3$** (**b**,**d**) at **B** = 0.5 T (**a**,**b**) and **B** = 1.0 T (**c**,**d**) (**k**,**B** ⊥ (111)). The solid lines are used solely as visual guides. Error bars represent ±2σ uncertainty in the integrated signal area.

The obtained U_{eff} value corresponds to the energy difference between the ground and the first excited states. This energy difference is sufficient to stabilize the toroidal spin state at low temperatures, and it is comparable to values reported for other trinuclear and hexanuclear Dy(III)-based SMTs[22,31,49].

Ab initio calculations

To further support the presence of toroidal magnetization in **R/S-Dy$_3$**, we employed ab initio computational methodologies previously used to reveal toroidal magnetism in Dy$_3$ triangles[23,50,51]. The methodology is based on applying multiconfigurational quantum chemistry methods (complete active space self-consistent field (CASSCF)/second-order complete active space perturbation/RASSI/SINGLE_ANISO, Supplementary Section 4). Supplementary Table 6 provides the calculated low-lying energy spectrum and the corresponding main values of the *g*-tensors of the Dy(III) sites in **R/S-Dy$_3$**, while Supplementary Table 7 gives the corresponding crystal field parameters for the ground atomic *J* multiplet of the Dy(III) sites. The crystal field splitting of the ground multiplet in **R/S-Dy$_3$** (about 390 cm^{-1} at CASSCF and 550 cm^{-1} at second-order complete active space perturbation) is smaller than that of the original Dy$_3$ triangle (about 700 cm^{-1} at CASSCF), as three axially coordinated Cl$^-$ ions produce additional transverse crystal field terms[23,50]. Despite this reduced axiality, the strong interaction between phenolate and Dy(III) ion yields a large ground state g_z (17.1–18.6) oriented nearly within Dy$_3$ plane (<3.4° deviation). Figure 2d and Supplementary Figs. 44 and 45 display the orientation of the ground-state main magnetic axes alongside the molecular frame, confirming the presence of toroidal magnetization. Therefore, the triangles investigated here have both a net spin magnetic moment **S** and a spin toroidal moment **T**. Their scalar product $\theta = \mathbf{S} \cdot \mathbf{T}$ serves as a chiral parameter defining the spin chirality of the triangle. In a given chiral crystalline structure, the two enantiomers of the Dy(III) triangles are not degenerate, and one spin triangle chirality will be energetically favoured over the other one. Note that $\mathbf{S} \cdot \mathbf{T}$ and $-\mathbf{S} \cdot -\mathbf{T}$ represent the same spin chirality. By favouring **S** over −**S**, for example by applying an external magnetic field, the crystalline chirality will then favour one sign of the toroidal moment over the other. Therefore, one of the two possible toroidal spin states was successfully favoured for each enantiomer by the structural chirality of the enantiopure ligands. The magnetic exchange interaction was considered in the Lines model, using a single parameter to describe the inter-site magnetic exchange interaction. Dipole–dipole interactions were included using ab initio computed on-site magnetic dipole operators. Best-fitted values for the Lines parameters describing magnetic exchange are −0.530 cm^{-1}/−0.405 cm^{-1} for **S-Dy$_3$** and −0.220 cm^{-1}/−0.220 cm^{-1} for **R-Dy$_3$** (Supplementary Table 8), in agreement with the values obtained by the BS-DFT approach (Supplementary Tables 9 and 10). The energy separation between the ground toroidal exchange state and the non-toroidal excited state is 4.7–5.7 cm^{-1} (Supplementary Table 8), which is comparable to that in the original Dy$_3$ (ref. 23) and that determined by μ-SQUID. Supplementary Figs. 19–22 compare the measured and calculated molar magnetization and magnetic susceptibility using the best-fitted magnetic exchange parameters, as determined by the POLY_ANISO software.

Supplementary Section 4 details the procedure developed to compute the unit-cell toroidal moment in **R/S-Dy$_3$**. All intramolecular exchange interactions are kept constant, while adjusting a single additional parameter that describes the inter-triangle magnetic interaction, which was found to be very weakly antiferromagnetic (−0.023 cm^{-1}) supported by the unique molecular packing. The magnetic dipole–dipole interaction was included for all metal pairs. The low-lying energy spectra of the entire unit cell of **S-Dy$_3$** and **R-Dy$_3$** are similar and grouped into five sets, depending on the number of Dy$_3$ triangles in the excited state (Supplementary Fig. 46). Supplementary Table 11 provides further details about the nature of their wave functions. The ground state of both compounds has a degeneracy of $2^4 = 16$, corresponding to coupling between large toroidal moments of the four molecules. Notably, the directions of toroidal moments of four molecules are the same (Supplementary Fig. 47 and Supplementary Tables 12 and 13), for example all pointing to axial Cl$^-$ ligands (**R-Dy$_3$**), symbolized by '+, +, +, +', or to axial water ligands (**S-Dy$_3$**), symbolized by '−, −, −, −' This indicates the formation of homochiral toroidal spin states at the unit-cell level, as computationally demonstrated here.

https://doi.org/10.1038/s41557-026-02070-4

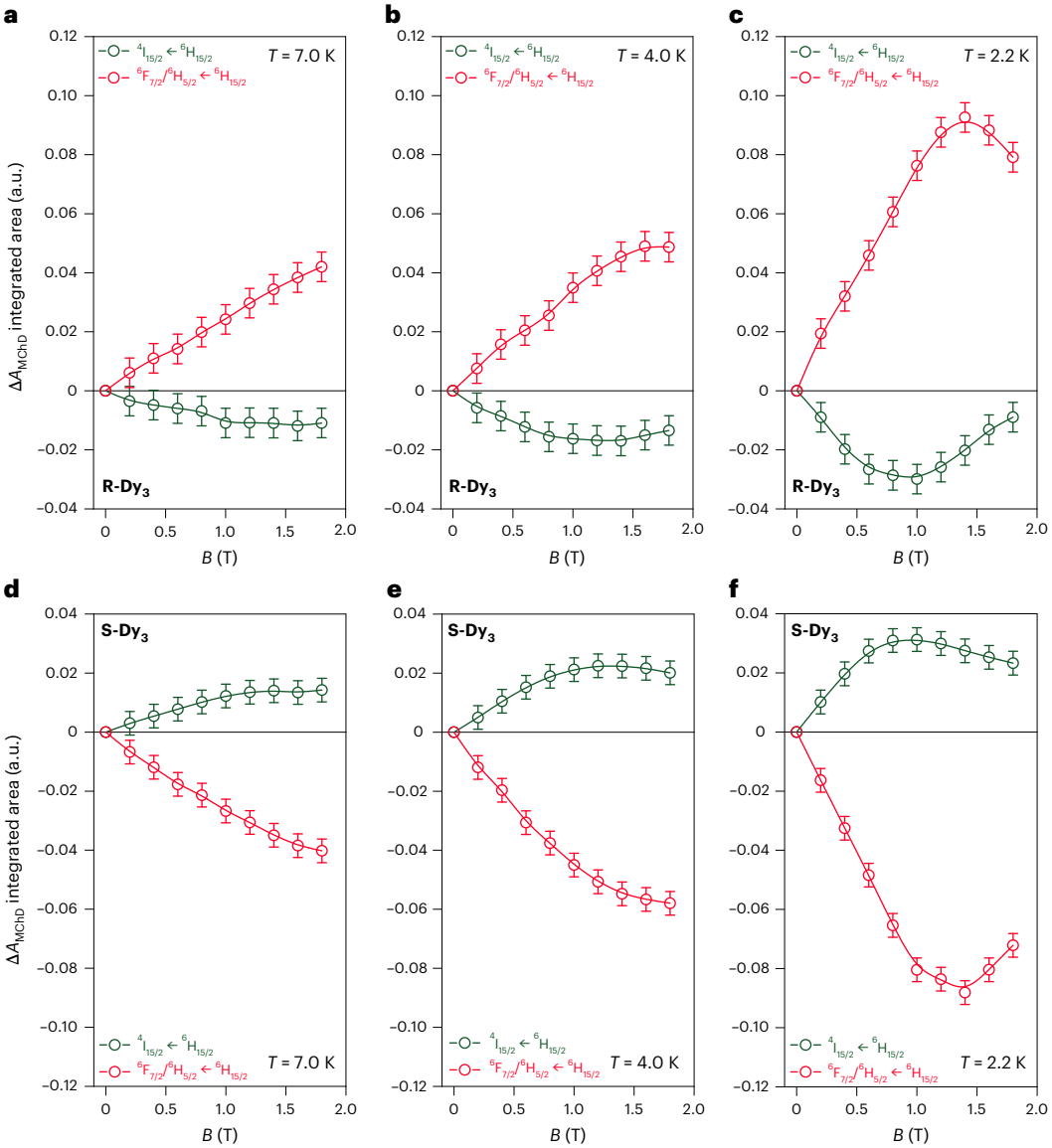

Fig. 6 | Magnetic field dependent MChD spectroscopy. a–f, Magnetic field dependence of MChD intensity (integrated absolute area of the MChD signals) for selected *f*–*f* transitions (see legend) at $T = 7.0$ K (**a**,**d**), 4.0 K (**b**,**e**) and 2.2 K (**c**,**f**) for **R-Dy$_3$** (**a**–**c**) and **S-Dy$_3$** (**d**–**f**) (**k**,**B** ⊥ (111)). The solid lines are used solely as visual guides. Error bars represent ±2σ uncertainty in the integrated signal area.

MChD spectroscopy

Variable-temperature (3.0–290 K) visible-near-infrared (400–1,600 nm) light absorption spectroscopy on oriented single crystals was used to get insights into the optical properties of **R/S-Dy$_3$**. Fine-structured absorptions associated with the *f*–*f* electronic transitions from the $^6H_{15/2}$ ground state to the various excited states manifolds of the Dy(III) ions are observed by lowering the temperature from 290 K to 3 K (Supplementary Fig. 49). The assignment of the observed transitions is reported in Supplementary Table 14. The energies and the absorption coefficients of the observed transitions are in good agreement with literature findings[52] (Supplementary Fig. 50).

Variable-temperature (2.2–50 K) and variable-magnetic-field (0–2.0 T) MChD spectroscopy was used to provide spectroscopic evidence of toroidal magnetic moments in these compounds. The collinear light wavevector **k** and magnetic field **B** were applied perpendicular and parallel to the (111) plane (Supplementary Fig. 17). When **k** and **B** ⊥ (111), one **Dy$_3$** molecule has its triangular plane parallel to (111), that is, its toroidal magnetic moment **T** is collinear to **k** and **B**. The three other **Dy$_3$** molecules have the triangular planes mainly perpendicular to (111) (roughly 70°), therefore their toroidal magnetic moments **T** are also perpendicular to **k** and **B**. MChD is sensitive to the magnetic moment projections collinear to the applied magnetic field. Therefore, when **k** and **B** ⊥ (111), the out-of-the-plane toroidal magnetic moment **T** of the Dy_3 molecule lying in the (111) plane can be probed together with the magnetic dipole moments contributions **S** of the three **Dy$_3$** molecules at 70° with respect to (111) because the magnetic easy axes of the Dy(III) are mainly on the triangular plane. On the contrary, when **k**,**B** || (111), the toroidal magnetic moment **T** of the **Dy$_3$** molecule lying on the (111) plane cannot be probed, being perpendicular to the magnetic field, while the magnetic dipole moments contributions **S** of Dy(III) ions associated with their magnetic easy axes are now probed. In this orientation, the three additional Dy(III) molecules have both **T** and **S** that are neither parallel nor perpendicular to **k**,**B** and oriented into different orientations as a consequence of the threefold symmetry. Therefore, along this orientation one can expect that the contribution to the MChD signal from these molecules is average to zero for both **T** and **S**.

Temperature-dependent MChD measurements with **k**,**B** ⊥ (111) were performed with an alternating magnetic field **B** = ±0.5 T. This

magnetic field intensity was selected to avoid saturation. The results are reported in Fig. 4.

MChD signals are observed for all *f*–*f* transitions probed by optical absorption. The relative intensity of ΔA_{MChD} with respect to the absorption coefficients *A* is evaluated by the dissymmetry factor g_{MChD} (Supplementary Equation 1) and the values are reported in Supplementary Table 14 for selected wavelengths at $T = 3.0$ K. Following with recent literature findings[52,53], the magnitude of the g_{MChD} values is in agreement with the electric-dipole induced character of the Dy(III) *f*–*f* transitions falling in the investigated range. For the sake of clarity, only the *f*–*f* transitions associated with the highest ΔA_{MChD} values will be discussed in the following, notably the $^6F_{11/2}/^6H_{9/2} \leftarrow {}^6H_{15/2}$ ($\lambda = 1{,}220$–$1{,}320$ nm), $^6F_{7/2}/^6H_{5/2} \leftarrow {}^6H_{15/2}$ (880–920 nm) and $^4I_{15/2} \leftarrow {}^6H_{15/2}$ (450 nm) transitions. In the 50–4.0 K range, all transitions behave similarly, gaining intensity as the temperature is lowered. This is the expected behaviour for a system of non-interacting paramagnetic spins (magnetic dipole moments)[52–56]. However, when the temperature is lowered further (<4.0 K), each transition shows a peculiar behaviour of the MChD signal: the $^6F_{7/2}/^6H_{5/2} \leftarrow {}^6H_{15/2}$ and $^4I_{15/2} \leftarrow {}^6H_{15/2}$ shows a regular monotonous behaviour down to 2.2 K; on the contrary, the $^6F_{11/2}/^6H_{9/2} \leftarrow {}^6H_{15/2}$ signal shows an abrupt decrease in MChD intensity between 4.0 K and 3.0 K (inset of Fig. 4a,b); finally, the $^6F_{5/2} \leftarrow {}^6H_{15/2}$ signal changes sign at 3.0 K and reaches its maximum positive value at 2.2 K. This unusual behaviour can be associated to the occurrence of a magnetic coupling at roughly 4.5 K between the Dy(III) ions forming the triangles and the change of the ground spin state from three non-interacting dipolar moments to a collective toroidal ground state.

Measurements performed on the opposite enantiomer provide mirror-image MChD spectra and the same temperature-dependent behaviour (Fig. 5a,b). Measurements performed under $\mathbf{B} = \pm 1.0$ T in the same *T* range shows similar MChD responses with higher intensity (Fig. 5c,d). Indeed, μ-SQUID measurements at $T = 2.2$ K, the lowest achievable temperature of the MChD experimental setup, show an increase of the overall magnetization as the magnetic field is increased from 0.5 T to 1.0 T without reaching saturation, in agreement with the observed MChD intensity increase.

Magnetic field dependent MChD measurements with $\mathbf{k},\mathbf{B} \perp (111)$ were performed with alternating magnetic field **B** in the 0–2.0 T range at $T = 7.0$ K, 4.0 K and 2.2 K. These temperatures were selected to be above (7.0 K), below (2.2 K) and at (4.0 K) the temperature at which the magnetic coupling between the Dy(III) ions overcomes thermal effects. Because the optical transparency of the **S-Dy$_3$** crystals was not suitable for measurements in the near-infrared range, in the following we will focus on the $^6F_{7/2}/^6H_{5/2} \leftarrow {}^6H_{15/2}$ and $^4I_{15/2} \leftarrow {}^6H_{15/2}$ transitions falling in the visible range that have high ΔA_{MChD} values at low temperature and a simple spectral shape. At $T = 7.0$ K, the magnetic field dependence of the MChD signals shows a linear increase with the magnetic field intensity for both transitions, as expected for a paramagnetic system of non-interacting spins (Fig. 6a). At $T = 4.0$ K, the magnetic field dependence changes. The $^6F_{7/2}/^6H_{5/2} \leftarrow {}^6H_{15/2}$ transition increases linearly and then starts to saturate at a **B** of roughly 1.3 T, while the $^4I_{15/2} \leftarrow {}^6H_{15/2}$ transition reaches a maximum at roughly 1.0 T and then starts to slightly decrease (Fig. 6b). When the temperature is lowered to 2.2 K, the $^6F_{7/2}/^6H_{5/2} \leftarrow {}^6H_{15/2}$ transition shows a maximum at roughly 1.3 T and then starts to decrease, while the maximum at roughly 1.0 T for the $^4I_{15/2} \leftarrow {}^6H_{15/2}$ transition already observed at 4.0 K is better evidenced, with an intensity that goes towards zero at 1.8 T (Fig. 6c). These behaviours are observed for both enantiomers with similar ΔA_{MChD} intensities and opposite sign (Fig. 6d–f).

The observation of a maximum at around 1.0–1.3 T for $T < 5$ K is indicative of a change of ground spin state occurring if a critical magnetic field is applied, in agreement with magnetic measurements. For the symmetry considerations (Fig. 2c), along the $\mathbf{k},\mathbf{B} \perp (111)$ orientation for $\mathbf{B} < 1.0$ T and $T = 2.2$ K, the toroidal spin state is expected to drive the MChD signal intensity. Indeed, the MChD signals gain intensity as the magnetic field increases, then, once the critical magnetic field is reached, the antiferromagnetic ground state associated with the toroidal moment competes with the non-toroidal excited state stabilized by the Zeeman effect where the spins are aligned along the direction of the magnetic field and the MChD signals lose intensity because the state associated with the toroidal moment is gradually depleted.

MChD measurements were performed with $\mathbf{k},\mathbf{B} \parallel (111)$ in the same temperature and field range. From the symmetry considerations (Fig. 2c), along this direction MChD spectroscopy should not be sensitive to the toroidal magnetic moment **T**. Indeed, temperature-dependent studies show MChD signals whose intensity increase in a similar way for all transitions down to the lowest temperature without any ΔA_{MChD} maximum or change in sign (Supplementary Fig. 51). Magnetic field dependence studies up to 1.8 T show a linear increase without saturation at $T = 4.0$ K and signals of higher intensity that start to saturate at 2.0 T at $T = 2.2$ K but without any maximum (Supplementary Fig. 52).

Conclusion

By designing homochiral hydrazide ligands that combine axial chirality and high coordination affinity for lanthanide ions, we successfully constructed a pair of Dy_3 SMT enantiomers. Within these homochiral molecules, the embedded structural chirality induces spin homochirality. The toroidal arrangement of magnetization in the ground state was probed by SQUID and μ-SQUID measurements on both polycrystalline samples and oriented single crystals. Ab initio calculations confirm non-coplanar spin texture within the molecular triangle and uniform spin chirality in the unit cell. Such homochiral SMTs are anticipated not only to achieve toroidal polarization without magnetic field gradients but also to facilitate the spectroscopic detection of the molecular toroidal ground state, owing to their intrinsic lack of inversion symmetry. The abrupt change in MChD intensity below the temperature at which the magnetic interaction favours the toroidal spin state and a decrease in MChD intensity above a critical magnetic field that suppresses the toroidal spin state evidences that MChD spectroscopy is sensitive to the magnetic coupling between the Dy(III) ions and the resulting toroidal magnetic moment. These results indicate that MChD spectroscopy appears as the technique of choice to provide experimental evidence of the toroidal moments orientation within the structure (toroidal spin texture) and correlate the toroidal moment orientation (spin chirality) with the absolute configuration of the system (structural chirality), key information that is inaccessible to thermodynamic techniques. Our work shows that Dy(III)-based triangles are excellent platforms to integrate structural chirality and spin chirality and to explore the interplay between magnetism and chirality. A uniaxial system where the molecular triangles crystallize all oriented along the same direction with a stronger magnetic coupling able to stabilize the toroidal spin states at higher temperature is thus expected to provide a greater toroidal polarization and a more straightforward spectral access to the toroidal magneto-chiral properties mentioned above.

Online content

Any methods, additional references, Nature Portfolio reporting summaries, source data, extended data, supplementary information, acknowledgements, peer review information; details of author contributions and competing interests; and statements of data and code availability are available at https://doi.org/10.1038/s41557-026-02070-4.

References

1. Mühlbauer, S. et al. Skyrmion lattice in a chiral magnet. *Science* **323**, 915–919 (2009).
2. Fert, A., Reyren, N. & Cros, V. Magnetic skyrmions: advances in physics and potential applications. *Nat. Rev. Mater.* **2**, 17031 (2017).

3. Yu, X. Z. et al. Transformation between meron and skyrmion topological spin textures in a chiral magnet. *Nature* **564**, 95–98 (2018).
4. Zheng, F. et al. Hopfion rings in a cubic chiral magnet. *Nature* **623**, 718–723 (2023).
5. Naaman, R., Paltiel, Y. & Waldeck, D. H. Chiral molecules and the electron spin. *Nat. Rev. Chem.* **3**, 250–260 (2019).
6. Matsukura, F., Tokura, Y. & Ohno, H. Control of magnetism by electric fields. *Nat. Nanotechnol.* **10**, 209–220 (2015).
7. Gaita-Ariño, A., Luis, F., Hill, S. & Coronado, E. Molecular spins for quantum computation. *Nat. Chem.* **11**, 301–309 (2019).
8. Nakajima, R. et al. Giant spin polarization and a pair of antiparallel spins in a chiral superconductor. *Nature* **613**, 479–484 (2023).
9. Kim, Y.-H. et al. Chiral-induced spin selectivity enables a room-temperature spin light-emitting diode. *Science* **371**, 1129–1133 (2021).
10. Göhler, B. et al. Spin selectivity in electron transmission through self-assembled monolayers of double-stranded DNA. *Science* **331**, 894–897 (2011).
11. Machida, Y., Nakatsuji, S., Onoda, S., Tayama, T. & Sakakibara, T. Time-reversal symmetry breaking and spontaneous Hall effect without magnetic dipole order. *Nature* **463**, 210–213 (2010).
12. Taguchi, Y., Oohara, Y., Yoshizawa, H., Nagaosa, N. & Tokura, Y. Spin chirality, berry phase, and anomalous hall effect in a frustrated ferromagnet. *Science* **291**, 2573–2576 (2001).
13. Zel'Dovich, Ia. B. Electromagnetic interaction with parity violation. *J. Exp. Theor. Phys.* **33**, 1531–1533 (1957).
14. Ederer, C. & Spaldin, N. A. Towards a microscopic theory of toroidal moments in bulk periodic crystals. *Phys. Rev. B* **76**, 214404 (2007).
15. Wang, W. et al. Spin chirality fluctuation in two-dimensional ferromagnets with perpendicular magnetic anisotropy. *Nat. Mater.* **18**, 1054–1059 (2019).
16. Pister, D., Irländer, K., Westerbeck, D. & Schnack, J. Toroidal magnetic molecules stripped to their basics. *Phys. Rev. Res.* **4**, 033221 (2022).
17. Van Aken, B. B., Rivera, J.-P., Schmid, H. & Fiebig, M. Observation of ferrotoroidic domains. *Nature* **449**, 702–705 (2007).
18. Talebi, N., Guo, S. & Aken, P. A. Theory and applications of toroidal moments in electrodynamics: their emergence, characteristics, and technological relevance. *Nanophotonics* **7**, 93–110 (2018).
19. Kubel, F., Crystal structure of lithium cobalt double orthophosphate, $LiCoPO_4$. *Z. Kristall.* **209**, 755 (1994).
20. Baum, M. et al. Controlling toroidal moments by crossed electric and magnetic fields. *Phys. Rev. B* **88**, 024414 (2013).
21. Ding, L. et al. Field-tunable toroidal moment in a chiral-lattice magnet. *Nat. Commun.* **12**, 5339 (2021).
22. Tang, J. et al. Dysprosium triangles showing single-molecule magnet behavior of thermally excited spin states. *Angew. Chem., Int. Ed.* **45**, 1729–1733 (2006).
23. Chibotaru, L. F., Ungur, L. & Soncini, A. The origin of nonmagnetic Kramers doublets in the ground state of dysprosium triangles: evidence for a toroidal magnetic moment. *Angew. Chem., Int. Ed.* **47**, 4126–4129 (2008).
24. Vignesh, K. R. & Rajaraman, G. Strategies to design single-molecule toroics using triangular $\{Ln_3\}_n$ motifs. *ACS Omega* **6**, 32349–32364 (2021).
25. Wang, Y.-X. et al. A single-molecule magnet assembly exhibiting a dielectric transition at 470 K. *Chem. Sci.* **3**, 3366–3370 (2012).
26. Vignesh, K. R. et al. Ferrotoroidic ground state in a heterometallic $\{Cr^{III}Dy^{III}_6\}$ complex displaying slow magnetic relaxation. *Nat. Commun.* **8**, 1023 (2017).
27. Fernandez et al. A Dy_4 cubane: a new member in the single-molecule toroics family. *Angew. Chem., Int. Ed.* **57**, 17089–17093 (2018).
28. Wu, J. et al. Realization of toroidal magnetic moments in heterometallic 3d-4f metallocycles. *Chem. Commun.* **54**, 1065–1068 (2018).
29. Wang, H. et al. Toroidal moment and dynamical control in luminescent 1D and 3D terbium calixarene compounds. *Chem. Sci.* **14**, 7208–7214 (2023).
30. Novitchi, G. et al. Heterometallic Cu^{II}/Dy^{III} 1D chiral polymers: chirogenesis and exchange coupling of toroidal moments in trinuclear Dy_3 single molecule magnets. *Chem. Sci.* **3**, 1169–1176 (2012).
31. Ungur, L. et al. Net toroidal magnetic moment in the ground state of a $\{Dy_6\}$-triethanolamine ring. *J. Am. Chem. Soc.* **134**, 18554–18557 (2012).
32. Spaldin, N. A., Fiebig, M. & Mostovoy, M. The toroidal moment in condensed-matter physics and its relation to the magnetoelectric effect. *J. Phys. Condens. Matter* **20**, 434203 (2008).
33. Hymas, K. & Soncini, A. Preparation and coherent manipulation of toroidal moments in molecules. Preprint at https://arxiv.org/abs/2504.08701 (2025).
34. Barron, L. D. & Vrbancich, J. Magneto-chiral birefringence and dichroism. *Mol. Phys.* **51**, 715–730 (1984).
35. Rikken, G. L. J. A. & Raupach, E. Observation of magneto-chiral dichroism. *Nature* **390**, 493–494 (1997).
36. Kumagai, N., Kanai, M. & Sasai, H. A career in catalysis: Masakatsu Shibasaki. *ACS Catal.* **6**, 4699–4709 (2016).
37. Spek, A. PLATON SQUEEZE: a tool for the calculation of the disordered solvent contribution to the calculated structure factors. *Acta Crystallogr. Sect. C* **71**, 9–18 (2015).
38. Petoud, S. et al. Brilliant Sm, Eu, Tb, and Dy chiral lanthanide complexes with strong circularly polarized luminescence. *J. Am. Chem. Soc.* **129**, 77–83 (2007).
39. Kahn, O. *Molecular Magnetism* (Wiley-VCH, 1993).
40. Blagg, R. J. et al. Magnetic relaxation pathways in lanthanide single-molecule magnets. *Nat. Chem.* **5**, 673–678 (2013).
41. Zhu, Z. et al. Air-stable chiral single-molecule magnets with record anisotropy barrier exceeding 1800 K. *J. Am. Chem. Soc.* **143**, 10077–10082 (2021).
42. Li, H.-Q. et al. Modulating the structures and magnetic properties of Dy(III) single-molecule magnets through acid–base regulation. *Inorg. Chem.* **61**, 2272–2283 (2022).
43. Guo, Y.-N. et al. Two-step relaxation in a linear tetranuclear dysprosium(III) aggregate showing single-molecule magnet behavior. *J. Am. Chem. Soc.* **132**, 8538–8539 (2010).
44. Guo, Y.-N., Xu, G.-F., Guo, Y. & Tang, J. Relaxation dynamics of dysprosium(III) single molecule magnets. *Dalton Trans.* **40**, 9953–9963 (2011).
45. Chow, C. Y. et al. Assessing the exchange coupling in binuclear lanthanide(III) complexes and the slow relaxation of the magnetization in the antiferromagnetically coupled Dy_2 derivative. *Chem. Sci.* **6**, 4148–4159 (2015).
46. Kaemmerer, H. et al. Inorganic approach to stabilizing nanoscale toroidicity in a tetraicosanuclear $Fe_{18}Dy_6$ single molecule magnet. *J. Am. Chem. Soc.* **142**, 14838–14842 (2020).
47. Paul, S. et al. Magnetization reversal across multiple serial barriers in a single Fe_3O_4 nanoparticle. *Phys. Rev. B* **105**, L180410 (2022).
48. Chauhan, D. et al. Ultraslow relaxation of toroidal state in ferrotoroidal dysprosium complex. *J. Am. Chem. Soc.* **147**, 39572–39581 (2025).
49. Lin, S.-Y. et al. Coupling Dy_3 triangles to maximize the toroidal moment. *Angew. Chem., Int. Ed.* **51**, 12767–12771 (2012).
50. Ungur, L., Van den Heuvel, W. & Chibotaru, L. F. Ab initio investigation of the non-collinear magnetic structure and the lowest magnetic excitations in dysprosium triangles. *New J. Chem.* **33**, 1224–1230 (2009).

51. Ungur, L., Lin, S.-Y., Tang, J. & Chibotaru, L. F. Single-molecule toroics in Ising-type lanthanide molecular clusters. *Chem. Soc. Rev.* **43**, 6894–6905 (2014).
52. Raju, M. S. et al. Magneto-chiral dichroism in a one-dimensional assembly of helical dysprosium(III) single-molecule magnets. *Inorg. Chem.* **62**, 17583–17587 (2023).
53. Raju, M. S. et al. Optical readout of single-molecule magnets magnetic memories with unpolarized light. *J. Am. Chem. Soc.* **146**, 23616–23624 (2024).
54. Shioukhi, I. et al. Magneto-chiral dichroism in a chiral twistacene ytterbium(III) one-dimensional assembly of single-molecule magnets. *Inorg. Chem. Front.* **12**, 5783–5791 (2025).
55. Adi, C. L. et al. Magneto-chiral dichroism of chiral lanthanide complexes in the context of Richardson's theory of optical activity. *Angew. Chem. Int. Ed.* **63**, e202412521 (2024).
56. Li, C.-Y. et al. Enhancement of magneto-chiral dichroism intensity by chemical design: the key role of magnetic-dipole allowed transitions. *J. Am. Chem. Soc.* **146**, 16389–16393 (2024).

Methods

Synthesis and characterization

Commercially available reagents were purchased from Energy Chemical and used without further purification. (*S*)-2,2′-diethoxy-(1,1′-binaphthalene)-6-carbaldehyde and (*R*)-2,2′-diethoxy-(1,1′-binaphthalene)-6-carbaldehyde were synthesized according to studies[57]. ^{1}H NMR spectra were recorded on 400 MHz Bruker spectrometer, AVANCE NEO 400 M, and chemical shifts are in δ units (ppm) with the residual solvent peak (δH = 2.50 ppm for $(CD_3)_2SO$). The coupling constant (*J*) is expressed in hertz (Hz). High-resolution ESI-MS spectra were recorded on a quadrupole time of flight SYNAPT G2 high-resolution mass spectrometer using electrospray ionization. SCXRD were measured using a Bruker Apex II CCD diffractometer with graphite-monochromatized Mo Kα radiation (λ = 0.71073 Å) at 180 K. Powder X-ray diffraction measurements were carried out on Bruker D8 advance X-Ray diffractometer (Cu-Kα radiation) at room temperature. Elemental analysis for C, H and N was measured using a Perkin-Elmer 2400 analyser. Fourier transform infrared data were collected on a Nicolet 6700 Flex Fourier transform infrared spectrometer equipped with a smart iTRTM attenuated total reflectance sampling accessory (4,000–525 cm^{-1}). Solution, powder and single-crystal magnetic data were collected on MPMS-XL-7 and μ-SQUID, respectively. The variable-temperature magnetic susceptibility measurement was collected with an external magnetic field of 1,000 Oe in the temperature range of 2–300 K. The d.c. magnetic susceptibility data are corrected for the diamagnetism estimated from Pascal's tables and sample holder calibration[58]. The a.c. susceptibility measurements were carried out under a 0 applied d.c. field and 3 Oe a.c. magnetic field at different temperature and frequency ranges. UV-vis spectra were recorded on a Shimadzu UV-2600 spectrometer. Natural circular dichroism spectra were collected on a Chirascan CD (Applied Photophysics) spectrometer. MChD spectra were recorded with an in-house built multichannel MChD spectrometer operating in the visible and near-infrared spectral window (400–1,600 nm) between 2.2 K and 290 K with alternating magnetic fields **B** up to ±2.0 T generated by a fast-sweeping superconducting magnet.

Synthesis of R-HL

A mixture of (*R*)-2,2′-diethoxy-(1,1′-binaphthalene)-6-carbaldehyde (1.11 g, 3 mmol) and 2-hydroxy-3-methoxybenzohydrazide (0.546 g, 3 mmol) in methanol (15 ml) was refluxed for 48 h. After cooling to the room temperature, the reaction mixture was concentrated and filtered to obtain the precipitate. The crude product was washed with cold methanol to give **R-HL** in 81% yield. ^{1}H NMR (400 MHz, $(CD_3)_2SO$): δ = 11.88 (*s*, 2 H), 8.58 (*s*, 1 H), 8.20 (*d*, *J* = 1.7 Hz, 1 H), 8.15 (*d*, *J* = 9.1 Hz, 1 H), 8.04 (*d*, *J* = 9.1 Hz, 1 H), 7.94 (*d*, *J* = 8.1 Hz, 1 H), 7.72–7.55 (*m*, 3 H), 7.47 (*dd*, *J* = 8.3, 1.4 Hz, 1 H), 7.33 (*t*, *J* = 7.4 Hz, 1 H), 7.24 (*t*, *J* = 7.5 Hz, 1 H), 7.16 (*d*, *J* = 7.6 Hz, 1 H), 7.04–6.85 (*m*, 3 H), 4.14–4.04 (*m*, 4 H), 3.81 (*s*, 3 H), 1.05–0.96 (*m*, 6 H). MS (ESI) calculated for $[M-H^+]^-$: 533.2, found: 533.4.

Synthesis of S-HL

S-HL was synthesized by a similar method to **R-HL** except that (*S*)-2,2′-diethoxy-(1,1′-binaphthalene)-6-carbaldehyde (1.85 g, 5 mmol) was used giving 83% yield. ^{1}H NMR (400 MHz, $(CD_3)_2SO$): δ = 11.87 (*s*, 2 H), 8.58 (*s*, 1 H), 8.20 (*s*, 1 H), 8.15 (*d*, *J* = 9.1 Hz, 1 H), 8.04 (*d*, *J* = 9.0 Hz, 1 H), 7.94 (*d*, *J* = 8.1 Hz, 1 H), 7.72–7.55 (*m*, 3 H), 7.48 (*d*, *J* = 7.9 Hz, 1 H), 7.33 (*t*, *J* = 7.5 Hz, 1 H), 7.24 (*t*, *J* = 7.6 Hz, 1 H), 7.16 (*d*, *J* = 7.8 Hz, 1 H), 7.04–6.85 (*m*, 3 H), 4.14–4.04 (*m*, 4 H), 3.81 (*s*, 3 H), 1.01 (*t*, *J* = 6.9 Hz, 6 H). MS (ESI) calculated for $[M-H^+]^-$: 533.2, found: 533.4.

Synthesis of R-Dy$_3$

A mixture of **R-HL** (53.4 mg, 0.1 mmol), $DyCl_3{\cdot}6H_2O$ (37.6 mg, 0.1 mmol) and Et_3N (21 μl, 0.15 mmol) in CH_3OH/CH_3CN (3 ml/12 ml) was stirred for 8 h at room temperature. The reaction mixture was filtered and the precipitate was collected. Then, the precipitate was dissolved in DMF. The single crystals of the complex suitable for SCXRD were obtained from slow diffusion of diethyl ether into DMF solution at room temperature after 1 week. Yield: 21 mg, 27%. Anal. Calculated for $C_{126}H_{170}Cl_4N_{15}O_{35}Dy_3$: C, 49.07; H, 5.56; N, 6.81. Found: C, 49.52; H, 5.688; N, 7.05. IR (cm^{-1}): 3,176(br), 2,977(w), 1,652(m), 1,616(s), 1,592(s), 1,553(s), 1,506(w), 1,453(w), 1,436(m), 1,384(w), 1,355(w), 1,315(m), 1,229(vs), 1,175(w), 1,148(w), 1,086(m), 1,044(s), 964(w), 913(w), 854(w), 795(s), 739(s), 657(w), 637(w), 625(w), 571(w), 567(w), 548(w), 544(w), 532(w).

Synthesis of S-Dy$_3$

S-Dy$_3$ was synthesized by a similar method to **R-Dy$_3$** except that **S-HL** was used. Yield: 23 mg, 30%. Anal. Calculated for $C_{126}H_{170}Cl_4N_{15}O_{35}Dy_3$: C, 49.07; H, 5.56; N, 6.81. Found: C, 49.41; H, 5.663; N, 6.96. IR (cm^{-1}): 3,194(br), 2,978(w), 1,651(m), 1,617(s), 1,592(s), 1,553(s), 1,505(w), 1,452(w), 1,436(m), 1,384(w), 1,356(w), 1,315(m), 1,229(vs), 1,174(w), 1,148(w), 1,091(m), 1,044(s), 964(w), 913(w), 854(w), 795(s), 740(s), 657(w), 637(w), 624(w), 598(w), 579(w), 564(w), 556(w), 540(w), 533(w), 529(w).

Data availability

Crystallographic data for the structures reported in this article have been deposited at the Cambridge Crystallographic Data Centre, under deposition numbers CCDC 2323094 (**S-Dy$_3$**) and CCDC 2323095 (**R-Dy$_3$**). Copies of the data can be obtained free of charge via the CCDC at https://www.ccdc.cam.ac.uk/structures. All other data are included in the paper or its Supplementary Information. Source data are provided with this paper and are also available via Figshare at https://doi.org/10.6084/m9.figshare.30937706 (ref. 59).

References

57. Wang, H. et al. Synthesis and fluorescence tuning of novel nitroxides with a binaphthyl framework. *Bull. Chem. Soc. Jpn* **84**, 341–343 (2011).
58. Boudreaux, E. A. & Mulay, L. N. *Theory and Applications of Molecular Paramagnetism* (John Wiley & Sons, 1976).
59. Zhu, Z. et al. Data for paper 'Homochiral toroidal spin state in Dy(III)-based single-molecule toroics'. *figshare* https://doi.org/10.6084/m9.figshare.30937706 (2025).

Acknowledgements

This work was supported by the National Natural Science Foundation of China (grant nos. 92261103 (J.T.) and 22201279 (Z.Z.)), the Key Research Program of Frontier Sciences, CAS (grant no. ZDBSLY-SLH023 (J.T)), the High-Level Talent Research Start-up Program of Beijing Institute of Technology (J.T.), the French National Research Agency (ANR) project SWITCH-MChD (grant no. ANR-23-CE07-0003 (M.A.)), the German Research Foundation DFG-CCR 1573 '4f for future' (S.P. and W.W.), the Gottfried Wilhelm Leibniz-Award no. ZVN-2020_WE 4458–5 (W.W.) and the Alexander von Humboldt Fellowship (W.W.). This work is also part of the LUMINESS project of PEPR LUMA and was supported by the ANR, as a part of the France 2030 program (grant no. ANR-24-EXLU-0006 (M.A.)). L.U. acknowledges the National University of Singapore for financing research projects A-8000079-00-00, and the Ministry of Education of Singapore for research project A-8001894-00-00. Ab initio calculations were performed on the ASPIRE-2A cluster (www.nscc.sg) under project 11004127. The computational resources of the HPC-NUS are gratefully acknowledged. We acknowledge Kubel F. for the data of $LiCoPO_4$ in the Crystallography Open Database.

Author contributions

J.T. conceived and designed the project. Z.Z., X.Y. and C.Z. performed the preparation and characterization. M.A., L.C.A., T.C. and G.L.J.A.R. carried out MChD characterizations. S.P. and W.W. conducted μ-SQUID measurements. E.J.M.C. and L.U. performed ab initio calculations. Z.Z., M.A., X.Y., J.T. and S.P. wrote the paper. All authors discussed the results.

Competing interests

The authors declare no competing interests.

Additional information

Supplementary information The online version contains supplementary material available at https://doi.org/10.1038/s41557-026-02070-4.

Correspondence and requests for materials should be addressed to Matteo Atzori or Jinkui Tang.

Peer review information *Nature Chemistry* thanks Dawid Pinkowicz and the other, anonymous, reviewer(s) for their contribution to the peer review of this work.